ACS OMEGA

Open Access

http://pubs.acs.org/journal/acsodf

Article

Geometric Analysis of Free and Accessible Volume in Atmospheric Nanoparticles

Panagiotis G. Mermigkis, Katerina S. Karadima, Spyros N. Pandis, and Vlasis G. Mavrantzas*

Cite This: *ACS Omega* 2023, 8, 33481−33492

Read Online

ACCESS | Metrics & More | Article Recommendations | Supporting Information

ABSTRACT: Computer-generated atomistic microstructures of atmospheric nanoparticles are geometrically analyzed using Delaunay tessellation followed by Monte Carlo integration to compute their free and accessible volume. The nanoparticles studied consist of *cis*-pinonic acid (a biogenic organic aerosol component), inorganic ions (sulfate and ammonium), and water. Results are presented for the free or unoccupied volume in different domains of the nanoparticles and its dependence on relative humidity and organic content. We also compute the accessible volume to small penetrants such as water molecules. Most of the free volume or volume accessible to a penetrant as large as a water molecule is located in the domains occupied by organics. In contrast, regions dominated by inorganics do not have any cavities with sizes larger than 1 Å. Solid inorganic domains inside the particle are practically impermeable to any small molecule, thereby offering practically infinite resistance to diffusion. A guest molecule can find diffusive channels to wander around within the nanoparticle only through the aqueous and organic-rich domains. The largest pores are observed in nanoparticles with high levels of organic mass and low relative humidity. At high relative humidity, the presence of more water molecules reduces the empty space in the inner domains of the nanoparticle, since areas rich in organic molecules (which are the only ones where appreciable pores are found) are pushed to the outer area of the particle. This, however, should not be expected to affect the diffusive process as transport through the aqueous phase inside the particle will be, by default, fast due to its fluid-like nature.

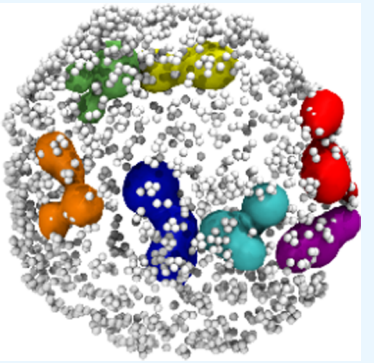

1. INTRODUCTION

The concept of free volume has been widely invoked over the years to describe the temperature dependence of viscosity in glass-forming systems near the liquid-glass transition temperature by correlating transport or relaxation with the amount of potentially compressible space available within the dense fluid.[1−5] The free volume is typically defined as the total volume of the system minus the volume occupied by the atoms of the system, the latter being defined as a hard-core volume and typically assumed to be temperature-independent.[5] In later studies,[6−14] the free volume concept was invoked to relate the diffusive motion of small penetrants in soft materials such as polymer melts and polymer glasses to a series of hopping events between sites where the penetrant can reside. Greenfield and Theodorou[12] implemented a geometric analysis to determine the accessible regions within a dense glassy polymer structure where a penetrant center may reside, how the size of these accessible regions changes with penetrant radius, how their shape is distributed, and how they are connected. This detailed information was exploited in a subsequent work[15] to study the diffusive motion of small spherical penetrants through glassy polymers by calculating the spectrum of rate constants describing the penetrant hopping motion as an activated process in the context of a multidimensional transition state theory (TST). In a more recent study,[16] the geometric analysis of Greenfield and Theodorou[12] was employed to determine the clusters of sites where a hard-sphere penetrant of a given radius (equal to a few Angstroms) can reside within polymer nanocomposite microstructures.

The geometric analysis starts by first decomposing thoroughly pre-equilibrated model structures of the material under study (in the form of periodic simulation cells) into nonoverlapping and space-filling Delaunay tetrahedra, then determining the free (unoccupied) volume in each tetrahedron, and finally identifying connected tetrahedra and their clustering to bigger entities (the so-called cavities). The calculation of free volume in each tetrahedron can be done either analytically[17] or, if the tetrahedra are highly irregular, by Monte Carlo integration.[18] Finally, the network of clusters formed and the diffusion pathways between neighboring sorption sites are determined by applying a connectivity algorithm.[12]

In the present work, we extend this detailed geometric analysis to model structures representative of atmospheric nanoparticles (NPs).[19,20] Our scope is to determine the

Received: May 11, 2023
Accepted: July 19, 2023
Published: September 7, 2023

distribution of empty space (free volume) in such particles as a function of relative humidity (RH) and degree of organic content, and from that, the accessible volume to molecules of a given size. This will be the first step toward analyzing the mechanism of diffusion (continuous versus jump-like) of small or large penetrants inside an atmospheric particle. Their diffusivity could be then determined either based on brute-force molecular dynamics (MD) simulations or on the basis of the spectrum of rate constants governing activated hopping events between clusters of free volume using multidimensional TST.[15] A recent MD study by Song et al.,[21] for example, has suggested that water diffusion in saccharide aerosol droplets is not continuous but, instead, it proceeds by discrete hops between transient cavities that form and dissipate due to thermal fluctuations in the highly viscous solution. Our work is more relevant for nanoparticles exposed to low levels of relative humidity because, as the water content of the nanoparticle increases, diffusion is expected to be dramatically facilitated due to the more fluid-like nature of the nanoparticle overall, resembling more and more a continuous process. In contrast, at low or intermediate relative humidity where the particle structure becomes more dense, more solid-like, and less permeable, the mode of diffusion can change, proceeding via a sequence of activated jumps between sorption sites connected with channels that open as a result of thermal fluctuations. This is at the heart of the present geometric analysis.

Atmospheric nanoparticles are highly complicated structures[22] not only because of the large number of constituent molecules but also because of the completely different morphologies and phases that can develop within them due to favorable or specific interactions between these species.[23] A large number of experimental, theoretical, and simulation studies over the years[24−44] have shown that these particles, which are complex multicomponent mixtures of organics, inorganics, and water, can exhibit nonideal behavior and undergo phase transitions and phase separation. In fact, Huang et al.[42] and Gaikwad et al.[43] have reported recently that particles consisting of primary and secondary organic aerosol, as well as secondary inorganic salts, can phase-separate even into three phases, depending on the elemental oxygen-to-carbon ratio of the secondary organic aerosol and relative humidity. The work confirmed the findings of a previous MD study,[20] which had indicated the development of three separate and chemically distinct domains inside nanoparticles less than 10 nm in diameter made of a mixture of organics, inorganic ions, and water molecules.

As a result of their highly complex and quite rich microstructure, molecular diffusion through an atmospheric nanoparticle can be an extremely complex process to directly simulate by resorting (e.g.,) to brute-force MD; thus, one needs to follow a more hierarchical strategy. As a first step toward such a multiscale approach for understanding molecular diffusion in atmospheric nanoparticles, we present here results from a detailed geometric analysis of the empty space (the so-called free or unoccupied volume) and its distribution in the three main domains that one typically expects inside such a particle: (a) solid (crystalline) core, (b) organic-rich phase, (c) aqueous phase. As a byproduct of this first analysis, we also obtain the volume accessible to a small penetrant inside the particle of size close to that of a water molecule and the connectivity of the corresponding sorption sites.

The remaining of the manuscript is organized as follows. In Section 2, we review the model particle structures analyzed (their composition and morphology) and provide details regarding the implementation of the geometric method for the determination of free volume from infinitely periodic systems already addressed so far to finite ones. This constitutes an important technical development. Section 3 presents the simulation results for the total volume, total surface area, and average shape of the various particles studied, the unoccupied and accessible volume in each one of them, and the corresponding network of cavities, including their distribution. We conclude with Section 4, summarizing the major findings of the work and discussing possible future developments.

2. METHODOLOGY AND SYSTEMS STUDIED

Five types of atmospheric nanoparticles were investigated (Table 1) consisting of 200 sulfate ions, 400 ammonium ions,

Table 1. Characteristics of the Five Different Atmospheric Nanoparticles Subjected to Geometric Analysis

system	number of organic molecules	number of water molecules	organic mass (%)	RH (%)	total number of atoms in the simulation cell
1	10	400	5	40	5090
2	200	400	52	40	10,600
3	400	400	69	39	17,000
4	400	1600	57	76	20,600
5	400	3200	47	89	25,400

several water molecules depending on the RH considered, and a variable number of *cis*-pinonic acid (CPA) ($C_{10}H_{16}O_3$) molecules. The five nanoparticles have been described and morphologically characterized in two previous studies[19,20] and correspond to systems with numbers 1, 14, 15, 18, and 19 in Table 1 of Karadima et al.[20] The simulation cells also contain nitrogen (N_2) and oxygen (O_2) molecules at the correct stoichiometry in order to represent the surrounding atmosphere and control the pressure. Systems 1−3 serve to examine the effect of organic mass (the number of organic molecules varies from 10 to 400, corresponding to a fraction of organic mass that extends from 5 to about 69%) at moderate to low RH (approximately 40%). Systems 4−5 serve to examine the impact of RH (by considering respectively 1600 and 3200 water molecules in the simulation cell) at constant organic content (number of organic molecules equal to 400). The system with 3200 water molecules in the simulation cell, in particular, is characterized by high RH, equal to 89%. All particles were studied at temperature T = 320 K and pressure P = 1 atm.[20] A temperature of 320 K is in the upper end of the atmospheric temperatures and is only used because the model particle structures that served as input to the geometric analysis had already been equilibrated at this temperature. However, we do not expect the results of the geometric analysis to change dramatically at somewhat lower (by 5−10%) temperatures. In fact, one should expect them to change proportionally to the change in the density of the nanoparticle with decreasing temperature.

For each one of the systems of Table 1, three independent configurations (borrowed from a previous long MD simulation per system[19]) were used for the geometric analysis by suitably adapting the algorithm developed by Mermigkis and Mavrantzas[16] for analyzing the free volume in a bulk polymer

https://doi.org/10.1021/acsomega.3c03293
ACS Omega 2023, 8, 33481−33492

nanocomposite. We worked only with three configurations per system because the results obtained from them were not that different, and for all NPs studied, they appeared internally consistent. To validate the results for the unoccupied/accessible volumes, we also simulated water and CPA as pure bulk systems at the same temperature and pressure conditions (T = 320 K and P = 1 atm).

An important difference between the systems analyzed in previous studies[12,16] and the nanoparticles addressed here is the finite size of the latter, which necessitated several modifications to the geometric algorithm. First, atoms in each of the five simulated NP systems are categorized as *internal* (i.e., atoms belonging to the NP) and *external* (i.e., atoms belonging to the surrounding atmosphere). *External* atoms include not only N_2 and O_2 molecules in the surrounding air but also CPA and water molecules that had escaped from the NP to the atmosphere in the course of the MD simulation (inorganic ions never came out from the NPs). Then, the geometric analysis starts by first tessellating the space inside the simulation cell into Delaunay tetrahedra by using as vertices the atomic positions in the system. Since *external* atoms are sparse, the number of atoms in the set S_i of atoms surrounding atomic site i that will lead to the formation of the Voronoi polyhedron around atom i (following the algorithm proposed by Tanemura et al.[45]) is equivalent to the total number of atoms in the system. This makes the entire procedure extremely slow from a computational point of view. In some cases, it was observed that the Delaunay tessellation could not even converge at all. We overcame this problem by adding a certain number of *ghost atoms* in the simulation cell around the nanoparticle in order to fill the surrounding gas-phase space; although ghost atoms are *external*, they are treated as system atoms in the course of the Delaunay tessellation.

In the next step, the tetrahedra formed in the course of the Delaunay tessellation are grouped into *internal* and *external*: *internal* tetrahedra have all of their vertices on atoms that belong to the NP, while *external* tetrahedra have at least one of their vertices outside the NP. The subset of *external* tetrahedra that have exactly three atoms on the surface of the NP are called *boundary external* tetrahedra. Similarly, the subset of *internal* tetrahedra sharing three vertices with an *external boundary* tetrahedron are called *boundary internal* tetrahedra. An interesting feature of *boundary* tetrahedra is that one of their faces can be used to locate the *boundary* atoms of the nanoparticle.

In the present analysis, the surface of the nanoparticle encompasses the *boundary* atoms, and thus it should not be confused with the nanoparticle surface region as defined by Karadima et al.[20] to denote the outer-most region of the nanoparticle. The total volume of the nanoparticle is equal to the sum of volumes of the individual *internal* tetrahedra, and its total surface is equal to the sum of the areas of the *boundary* faces of all *boundary internal* tetrahedra. From the detailed tessellation of the volume of each nanoparticle into Delaunay tetrahedra, we can also get information about the shape of the nanoparticle by looking at the positions of its *boundary* atoms. For example, we can compute the equivalent radius of gyration, the dimensionless asphericity b,[12] and the relative shape anisotropy[11] κ^2 of the nanoparticle.

The third step in the geometric analysis is to characterize the formed Delaunay tetrahedra by considering the nature of atoms defining their vertices so that we can assign them to one of the three regions making up the particle: the *core*, the *organic phase*, and the *aqueous phase*. If all vertices correspond to atoms of the same compound (e.g., they are all organic or inorganic (sulfate or ammonium ions) or water atoms), the corresponding tetrahedron is categorized as a *pure organic CPA* or *pure inorganic* or *pure water tetrahedron*; otherwise, it is an *interfacial tetrahedron*. The *total volume* of a nanoparticle region, either *pure* or *interfacial*, is obtained by summing the volumes of the corresponding tetrahedra spanning that region.

Once space has been tessellated into tetrahedra, the next step is to calculate the *free* or *unoccupied* volume in the nanoparticle or its volume that is *accessible* to a penetrant of a given radius. For each *internal* tetrahedron, these calculations are performed by Monte Carlo integration (with about 30,000 samplings per tetrahedron), exactly as described by Mermigkis and Mavrantzas,[16] while for each *external* tetrahedron, we assume that the *unoccupied* or the *accessible volume* is by definition zero. We can also use information about the connectedness of tetrahedra to define the clusters (extended regions) of accessible volume inside the nanoparticle that are accessible to a guest molecule.[12,16] We assume that these clusters are made exclusively of *internal* tetrahedra that never cross the large empty space of gas molecules surrounding the particle, even if the cluster is terminated by a *boundary internal* tetrahedron of an *accessible* (to the chosen penetrant) *boundary* face.

Having defined the total volume of the nanoparticle (V^{T}) or the total unoccupied volume (V^{unoc}) or the total accessible volume to a penetrant of radius r_{p} ($V^{\mathrm{acc}}_{r_{\mathrm{p}}}$), the final step of the geometric analysis is to calculate how these volumes are distributed within the nanoparticle. Strictly mathematically, and on the basis of the present classification, one can consider seven (7) different types of regions within a nanoparticle, which we can label with the symbol k: k = 1 corresponding to a *pure organic* domain, k = 2 corresponding to a *pure (dry or solid) inorganic* domain, k = 3 corresponding to a *pure aqueous* phase, k = 4 corresponding to an *organic−inorganic interface*, k = 5 corresponding to an *organic−water interface*, k = 6 corresponding to an *inorganic−water interface*, and k = 7 corresponding to a *triple interface*. However, when we calculate the total or accessible volume of a *nanoparticle region* (solid core, organic-rich, aqueous with dissolved inorganics), we should incorporate into it the corresponding total or accessible volume located at its interfaces; thus, in the following, only values of k from 1 to 3 will appear with the understanding that the corresponding domain includes also the relevant interfacial contributions. For example, the total volume of organic-rich domains is given as

$$V^{\mathrm{T}}_{\mathrm{org,inc}} = V^{\mathrm{T}}_{\mathrm{org}} + \sum_{i=1}^{N^{\mathrm{org-inorg}}} \frac{\kappa_{i,\mathrm{org}}}{4} V^{T}_{i,\mathrm{org-inorg}} + \sum_{i=1}^{N^{\mathrm{org-water}}} \frac{\lambda_{i,\mathrm{org}}}{4} V^{\mathrm{T}}_{i,\mathrm{org-water}} + \sum_{i=1}^{N^{\mathrm{triple}}} \frac{\mu_{i,\mathrm{org}}}{4} V^{\mathrm{T}}_{i,\mathrm{org-triple}} \quad (1)$$

where $V^{\mathrm{T}}_{\mathrm{org}}$ denotes the nanoparticle volume residing in domains dominated by the *organic* components while $V^{\mathrm{T}}_{i,\mathrm{org\text{-}inorg}}$, $V^{\mathrm{T}}_{i,\mathrm{org\text{-}water}}$, and $V^{\mathrm{T}}_{i,\mathrm{org\text{-}triple}}$ stand for the nanoparticle volume found in *organic−inorganic*, *organic−water*, and *organic−inorganic−water* (*triple*) *interfaces*, respectively, with $\kappa_{i,\mathrm{org}}$, $\lambda_{i,\mathrm{org}}$, and $\mu_{i,\mathrm{org}}$ denoting the respective number of atoms (or vertices) of the i-th tetrahedron belonging to organic species in these domains. Also, $N^{\mathrm{org-inorg}}$, $N^{\mathrm{org-water}}$ and N^{triple} denote the

https://doi.org/10.1021/acsomega.3c03293
ACS Omega 2023, 8, 33481−33492

number of tetrahedra belonging to an organic−inorganic, organic−water and triple interface, respectively. Similarly, the corresponding *accessible volume* in organic-rich regions including all possible *interfacial* contributions is given as

$$V_{\mathrm{org,inc}}^{\mathrm{acc}} = V_{\mathrm{org}}^{\mathrm{acc}} + \sum_{i=1}^{N^{\mathrm{org-inorg}}} \frac{\kappa_{i,\mathrm{org}}}{4} V_{i,\mathrm{org-inorg}}^{\mathrm{acc}} + \sum_{i=1}^{N^{\mathrm{org-water}}} \frac{\lambda_{i,\mathrm{org}}}{4} V_{i,\mathrm{org-water}}^{\mathrm{acc}} + \sum_{i=1}^{N^{\mathrm{triple}}} \frac{\mu_{i,\mathrm{org}}}{4} V_{i,\mathrm{org-triple}}^{\mathrm{acc}} \quad (2)$$

and the same for the total volume and total accessible volume in the other two primary domains (inorganic-rich and aqueous).

Let us indicate with N^k the number of tetrahedra found in a domain that is of the k-th type. Then, the *fraction* of total nanoparticle volume residing in a domain of type k is

$$f_k^{\mathrm{T}} = \frac{\sum_{i=1}^{N^k} V_{i,k}^{\mathrm{T}}}{V^{\mathrm{T}}} \quad (3)$$

where $V_{i,k}^{\mathrm{T}}$ denotes the volume of the i-th tetrahedron that happens to be in this (k-th) domain. Similarly, the *fraction* of the total accessible nanoparticle volume to a penetrant of radius r_{p} in a domain of type k is

$$f_k^{\mathrm{acc}} = \frac{\sum_{i=1}^{N^k} V_{i,k}^{\mathrm{acc}}}{V^{\mathrm{acc}}} \quad (4)$$

where $V_{i,k}^{\mathrm{acc}}$ denotes the *accessible volume* of the i-th tetrahedron that happens to be in this (k-th) domain.

The *fraction* of *unoccupied* or *accessible volume* in a given region of the particle is also of interest, since it provides information about the percentage of volume of that region that is accessible to a penetrant of a given radius. Following the formalism of Mermigkis and Mavrantzas,[16] this fraction is computed according to

$$\varphi_k^{\mathrm{acc}} = \frac{\sum_{i=1}^{N^k} V_{i,k}^{\mathrm{acc}}}{\sum_{i=1}^{N^k} V_{i,k}^{\mathrm{T}}} = \frac{V_k^{\mathrm{acc}}}{V_k^{\mathrm{T}}} \quad (5)$$

where V_k^{acc} is the total *accessible volume* within domains of type k, while $V_k^{\mathrm{T}} = f_k^{\mathrm{T}} V^{\mathrm{T}}$ is the total volume of these domains.

A nice feature of the geometric algorithm is that it can also track the connectivity of tetrahedra formed in order to detect small *islands* inside the nanoparticle containing exclusively a certain type of molecules. This is achieved as follows: for a given compound, say A (e.g., an organic, inorganic, or a water molecule), and starting from a vertex of a *pure* tetrahedron of this compound, we construct a graph whose nodes correspond to vertices of tetrahedra which have at least two atoms belonging to A (in the case of a neighboring tetrahedron with only one vertex of A, the island will have a *boundary* atom, and so the edge of the graph will be a terminal node). Given a node of the graph (and thus a vertex of a tetrahedron), we follow the vertices of the tetrahedra sharing the same node and belonging to A to identify all of those nodes that do not form a closed loop (i.e., they do not return to a node having already been visited). The algorithm is terminated when the cycle has been completed, i.e., when the path has returned to the starting vertex.

The methodology followed to identify the formation of *islands* does not necessarily assume that the full set of atoms (vertices) belong to *pure* tetrahedra, since a narrow sequence of atoms of an *island* can pass through an interfacial tetrahedron as long as this contains at least two atoms (vertices) that belong to molecules of type A. The total volume of the formed *island* is then

$$V_{\mathrm{island}}^{\mathrm{T}} = \sum_{i=1}^{N^{\mathrm{island}}} \frac{n_i}{4} V_i^{\mathrm{T}} \quad (6)$$

where N^{island} denotes the total number of tetrahedra in an *island* of compound A, V_i^{T} is the volume of the i-th tetrahedron participating in the formation of the *island*, and n_i is the number of vertices of the i-th tetrahedron that belong to a compound of type A. The density of an *island* is computed from the masses of atoms on the vertices at its tetrahedra and its volume, $V_{\mathrm{island}}^{\mathrm{T}}$. The volume-weighted mean density of *islands* of compound A, $\langle \rho_{\mathrm{A}} \rangle_V$, is then extracted through an equation similar to eq. 23 in Mermigkis and Mavrantzas[16] for the volume-weighted distribution (i.e., the one based on the total volume *fraction* and not on the *accessible volume fraction*). The density of an island can be slightly different from the density of the corresponding pure compound at the same conditions due to density variations in the *interfacial* areas that contribute to the total volume of some narrow island domains. This is more pronounced for compounds spread to relatively small islands inside the nanoparticle, since *interfacial* regions then make a larger contribution to the total volume of the island. The identification of islands gives a picture of how extended the three characteristic regions making up the atmospheric particle (core or inorganic-rich, organic-rich, aqueous with dissolved inorganics) are and how they are spread within the nanoparticle.

3. RESULTS AND DISCUSSION

3.1. Spatial Distribution of Nanoparticle Components. Except for the nanoparticle of System 1 which contains only a small fraction of organic mass, organic molecules in all other nanoparticles are organized into one single *island*. The same is true for the inorganic content at low RH, but as the RH increases, more and more smaller domains containing the inorganic species appear. In the particle of System 5 which is at the highest RH, water molecules are dispersed almost everywhere within the nanoparticle, forming large aqueous islands in which inorganic species are dissolved.[20] In the snapshot shown in Figure 1a, we can observe one large core of inorganic ions and fourteen significantly smaller ones. The colors in the figure denote different islands whose atoms, in all cases, are made up of inorganic ions; white beads, on the other hand, denote the surface atoms (irrespective of their chemistry). The corresponding islands of aqueous phases formed in the case of the nanoparticle at the highest RH (System 5) are shown in Figure 1b, where the different colors denote different islands, all of which are made now by water molecules, while the white beads denote again the surface atoms (irrespective of their chemistry). Here, water and inorganic ions prefer to be together in small regions at the core of the particle because of the salting-out effect. A similar conclusion had been reported by Karadima et al.[20] through a different analysis. A small degree of mixing between organic

https://doi.org/10.1021/acsomega.3c03293
ACS Omega 2023, 8, 33481−33492

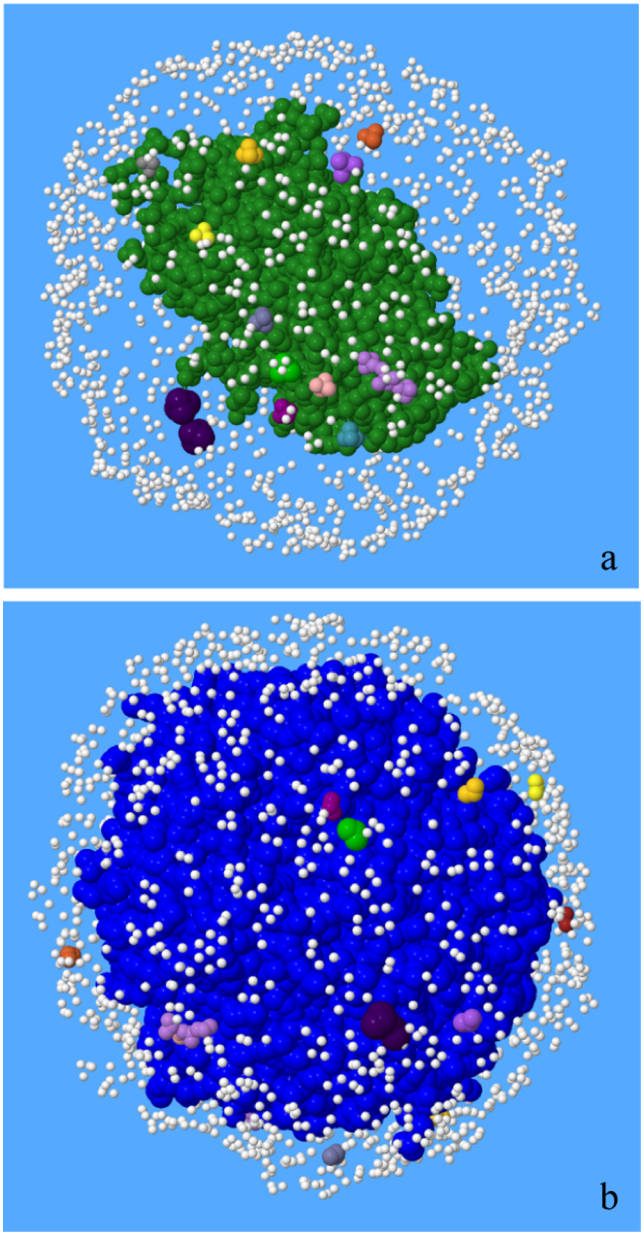

Figure 1. Visualization of (a) inorganic-rich (representative of the solid core) and (b) water-rich (representative of the aqueous phase) *islands* in the nanoparticle of System 5 containing 47% CPA at 89% RH. The color used to distinguish different *islands* was selected randomly from a set of ten different colors, which explains why some of the *islands* have received the same color. White dots represent the *boundary* atoms.

and water molecules is also evident in the same figure.[20] Inorganic ions and water islands form similar islands also in the case of the nanoparticle of System 4, confirming its "core−shell/organic surface" morphology.[20]

For the nanoparticle of System 3 (CPA 69%, RH 39%), all organic species prefer to be at its outer area, forming one single island, while inorganic species form two separate islands (two solid cores) in its interior, indicative of a "core−shell/organic surface with inorganic inclusions" morphology,[20] as depicted in Figure 2. On the other hand, in the nanoparticle of System 1 (low organic mass and low RH), the organic content is again found at its outer area, but now this is dispersed in five different islands. Inorganic species, on the other hand, form a

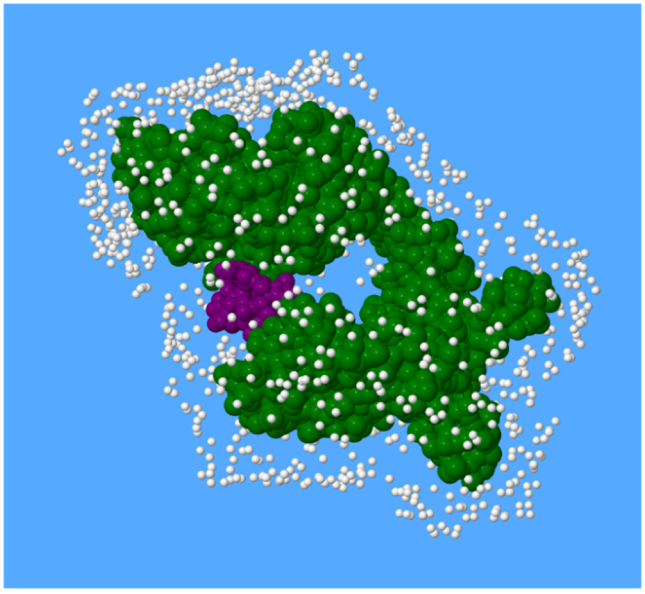

Figure 2. Visualization of the two inorganic-rich *islands* in the nanoparticle of System 3 containing 69% CPA at 39% RH. White small dots represent the *boundary* atoms. The two islands are located at the core of the nanoparticle. We also clarify that the two different islands are separate and do not share any common tetrahedra (although it appears so in the figure due to the relatively large size of the beads we used to represent more clearly the atoms in the two islands).

single island at the core of the particle, indicating the so-called "organic-enriched surface with islands"[20] morphology (Figure 3). Overall, and as we move from particles at high or medium RH (Systems 5 and 4) to systems at low RH (Systems 3 and 2), the aqueous phase does not include one single domain but appears to be broken into a larger number of smaller islands spread everywhere within the particle (Figure 4).

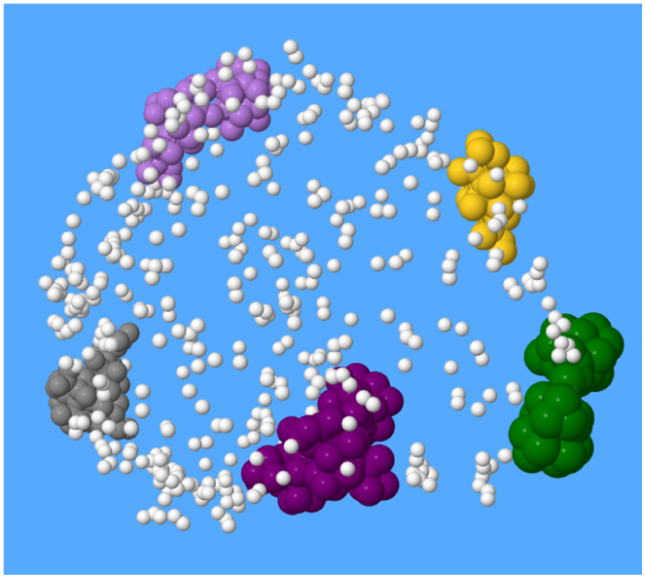

Figure 3. Visualization of organic-rich *islands* in the nanoparticle of System 1 containing 5% CPA at 40% RH. With different colors, we denote different islands in the nanoparticle, each one containing only organic species. The *boundary* atoms are denoted as small white beads.

https://doi.org/10.1021/acsomega.3c03293
ACS Omega 2023, 8, 33481−33492

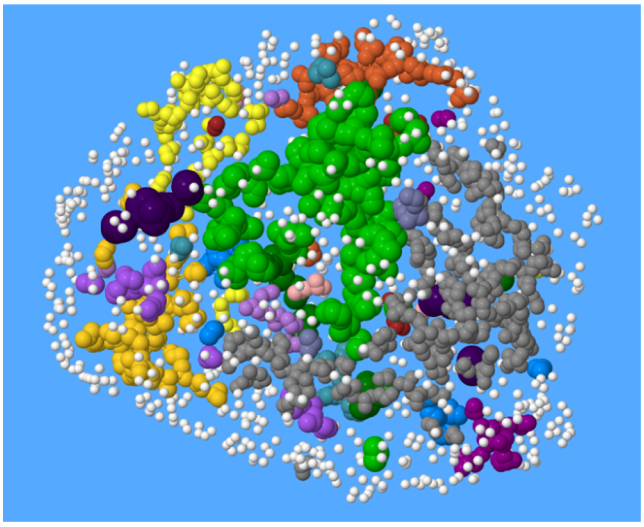

Figure 4. Visualization of water-rich *islands* in the nanoparticle of System 2 containing 52% CPA at 40% RH. The islands are found both at the outer areas and at the core of the particle. Different colors denote different water *islands* except for the white small beads which denote the *boundary* atoms.

Due to the small spatial extent of the different *islands* that exist inside the particle, the corresponding mean densities of the three major structures (inorganic solid core, organic-rich, aqueous phase) are slightly different from system to system. For example, the mean volume-weighted density of the organic phase formed in the smallest nanoparticle (System 1) is around 10% higher than in the systems with larger organic *islands* (Table 2). This also explains the relatively large error bars accompanying these data (calculated by examining 3 different configurations per nanoparticle). For comparison, the density of bulk CPA in its amorphous solid state at T = 320 K (melting point between 340 and 377 K[46]) and pressure P = 1 atm is 1.066 g/cm^3. On the other hand, regions occupied mostly by inorganic ions exhibit higher densities. When these species form one big core under conditions of low RH (Systems 1 and 2), their density becomes identical to that of bulk crystalline ammonium sulfate (1.77 g/cm^3).[47] Finally, the density of the aqueous phase within the nanoparticle is slightly higher than that of pure bulk water under the same temperature and pressure conditions ($\rho_{\text{bulk water}}$ = 0.984 ± 0.005 g cm^{-3}).[48] The small discrepancy is a numerical artifact related to fluctuations in the size of the different droplets forming in the various particles.

3.2. Total Volume, Total Surface Area, and Average Shape of the NP. The results from the detailed geometric analysis for the total volume V^{T}, the equivalent diameter D_{eq},[20] and the shape of the studied particles agree with those reported by Karadima et al.[20] (Table 3) even if a totally different methodology (calculation of the three major semi-axes of the nanoparticle from its mass inertia tensor) was used. The distribution of total nanoparticle volume (prior to subtracting any atomic volumes to compute the free volume) into the three nanoparticle phases is based on the knowledge of the *fractions* f_k^{T}, and for the five examined systems is presented in Figure S1 of the Supporting Information.

The anisotropy of the nanoparticle is characterized by the relative shape anisotropy parameter κ^2, which was less than 0.1 for all five particles studied, indicating that all of them are quite symmetric. We also computed the dimensionless asphericity b to check if the nanoparticles are spherical-like ($b \sim 0$) or ellipsoidal-like ($b \sim 0.5$). All of the results of the shape analysis are shown in Table 3 and indicate that the smaller particles or the particles at low RH tend to be ellipsoidal, while particles at a higher RH are practically spherical. In general, increasing the organic content (Systems 1−3) increases the size of the particle without substantially affecting its shape, as most of the organic molecules prefer to reside at the outer surface. At conditions of high RH (Systems 4 and 5), organic molecules still migrate to the surface of the particle,[20] but the particle swells considerably because of the increased water content, which enhances sphericity.

The mean total surface area of the particles studied and their interfacial composition are shown in Table 4. The boundary area of the largest particle studied here (System 5), which is practically spherical (see asphericity value in Table 3), is a little higher compared to the corresponding sphere of the equivalent diameter (equal to 7.6 nm from Table 3), which comes out to be 181.36 nm^2. This is attributed to the roughness of its outer surface, as revealed by our detailed geometric analysis. Furthermore, and with the exception of the system with the lowest organic content (System 1), the surface of the nanoparticles is dominated by organic molecules. Increasing the organic mass (Systems 1−3) enhances the presence of organics at the surface, while inorganic ions are totally absent.

3.3. Unoccupied/Accessible Volume in Each Nanoparticle. The total *fraction* of *unoccupied* volume and the total volume *accessible* to a water penetrant in the atmospheric particles examined in this work are presented in Table 5. In general, the *total unoccupied volume fraction* φ^{unoc} (the volume accessible to a pseudo-penetrant of zero radius) in the nanoparticles is between 0.22 and 0.26, while the total *accessible volume fraction* for a penetrant of the size of a water molecule $\varphi^{\text{acc}}_{\text{water}}$ ($r_{\text{p}} = r_{\text{w}}$ = 1.4 Å) is between 0.0048 and 0.011. The latter is a very small fraction, implying that diffusion of such a molecule in the nanoparticle is not a continuous process, but most likely, it involves a sequence of activated jumps or hopping events from one site of accessible volume to another. The value of φ^{unoc} in the particles increases with increased fraction of organic content (Systems 1−3), an

Table 2. Average Number of *Islands* per Nanoparticle and Mean Volume-Weighted Densities of the Three Major Phases (Organic, Inorganic or Core, Aqueous) Present in the Five Simulated Systems

system	number of organic-phase islands	number of inorganic-phase islands	number of aqueous-phase islands	mean density of organic phase (g cm^{-3})	mean density of inorganic phase (g cm^{-3})	mean density of aqueous phase (g cm^{-3})
1	5	1	16	1.266 ± 0.156	1.768 ± 0.002	1.038 ± 0.032
2	1	1	38	1.122 ± 0.029	1.765 ± 0.002	1.011 ± 0.078
3	1	2	60	1.057 ± 0.003	1.788 ± 0.007	1.003 ± 0.076
4	1	4	37	1.080 ± 0.008	1.813 ± 0.078	1.033 ± 0.045
5	1	15	22	1.076 ± 0.017	1.843 ± 0.185	1.032 ± 0.026

https://doi.org/10.1021/acsomega.3c03293
ACS Omega 2023, 8, 33481−33492

Table 3. Results from the Geometric Analysis for the Total Volume V^T, the Equivalent Diameter D_{eq}, the Relative Shape Anisotropy κ^2, and the Dimensionless Asphericity b of the Particles Studied Here, and Comparison with the Corresponding Results of Karadima et al.[20]

system	number of organic molecules	number of water molecules	D_{eq} [20] (nm)	D_{eq} (nm)	V^T (nm^3)	κ^2 [20]	κ^2	b
1	10	400	4.3	4.4	38.7	0.07	0.06	0.22
2	200	400	5.6	5.9	91.2	0.09	0.07	0.21
3	400	400	6.8	7.1	125.1	0.09	0.06	0.22
4	400	1600	6.9	7.1	183.4	0.01	0.006	0.07
5	400	3200	7.5	7.6	230	0.00	0.003	0.04

Table 4. Total Surface Area and Surface Composition Based on the Fraction of *Boundary* Atoms Belonging to Organic Molecules, Inorganic Ions, and Water Molecules from the Geometric Analysis of This Work

system	surface area (nm^2)	percentage of organic boundary atoms (%)	percentage of inorganic boundary atoms (%)	percentage of water boundary atoms (%)
1	68.44	17.4	9.6	73
2	125.37	91.3	0.6	8.1
3	174.59	99.5	0	0.5
4	182.61	97.1	0	2.9
5	212.45	97	0	3

Table 5. Total *Fraction of Unoccupied Volume* and Total *Fraction of Volume Accessible* to a Water Molecule in the Five Simulated Atmospheric Particles

system	φ^{unoc}	φ^{acc}_{water}
1	0.225	0.0048
2	0.232	0.0067
3	0.25	0.0109
4	0.25	0.0051
5	0.261	0.0052

indirect indication that organic-rich islands contribute substantially to the formation of voids. The same is true for φ^{acc}_{water}. For the nanoparticle with the highest RH (System 5), φ^{unoc} is slightly higher due to the dominance of aqueous solution domains. In contrast, as the RH increases, φ^{acc}_{water} decreases (compare, e.g., System 3 and Systems 4 and 5). To explain this, we also computed φ^{acc}_{water} for bulk water and found it to be equal to 0.00014, which is indeed a very small number, indicating that water molecules form a dense structure due to their tight hydrogen-bonding network. Of course, this is purely a *geometric* and *static* result referring to how water molecules are organized in their liquid state and does not imply anything about the diffusive process, since small molecule diffusivity in an aqueous solution is, by default, a fast process due to the liquid-like nature of water at room conditions (compared to inorganics that form practically solid structures or to organics that are either glassy or highly viscous materials).

The *fraction* f^{unoc}_k of *total unoccupied volume* in different regions of the nanoparticle (inorganic-rich, organic-rich, aqueous phase) is depicted in Figure S2 of the Supporting Information. Figure S2 shows the contribution of each region to the total measured *unoccupied volume*, and the overall picture is similar to that extracted from the corresponding distribution of the total particle volume (Figure S1). For instance, except for the smallest nanoparticle containing only ten organic molecules (System 1), most of the *unoccupied volume* within a nanoparticle resides in organic-rich regions ($f^{unoc}_{organic} \geq 0.5$), which is directly connected with the corresponding *fraction* of total particle volume analyzed earlier. This becomes more pronounced when we study the distribution of the total *accessible volume* (e.g., to a penetrant such as water, $r_p = r_w$) in the three characteristic nanoparticle regions (Figure 5). Apart from System 1, organics dominate

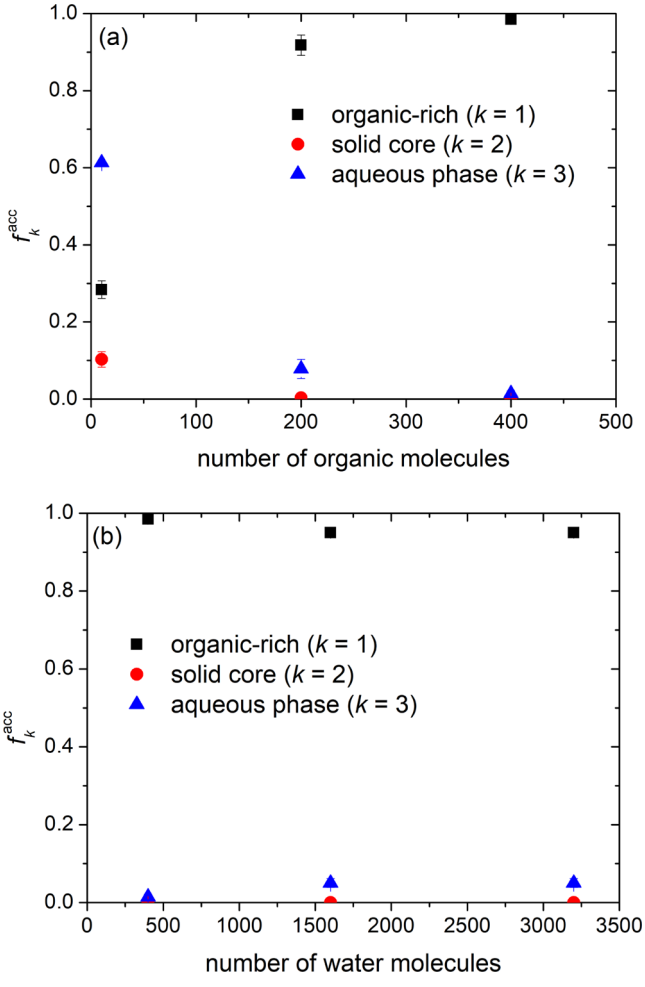

Figure 5. Fraction of total *accessible volume* for $r_p = r_w$ in organic-rich, inorganic-rich, and water-rich regions, as a function of nanoparticle content in (a) organic and (b) water molecules.

completely the cavities accessible to external penetrants in all nanoparticles ($f^{acc}_{organic} > 0.9$); domains rich in inorganic ions and water, on the other hand, contribute practically zero to the *accessible volume*. Because of the small φ^{acc}_{water} in each particle, the total *accessible volume* in small particles is very small (smaller than 0.5 nm^3 in the NPs of Systems 1 and 2), which

https://doi.org/10.1021/acsomega.3c03293
ACS Omega 2023, 8, 33481−33492

also explains why the contributions to f_k^{acc} in the smallest particles (System 1 and 2) are characterized by large uncertainties.

The corresponding results for the *fraction* of *unoccupied volume* are depicted in Figure 6. The results extracted from

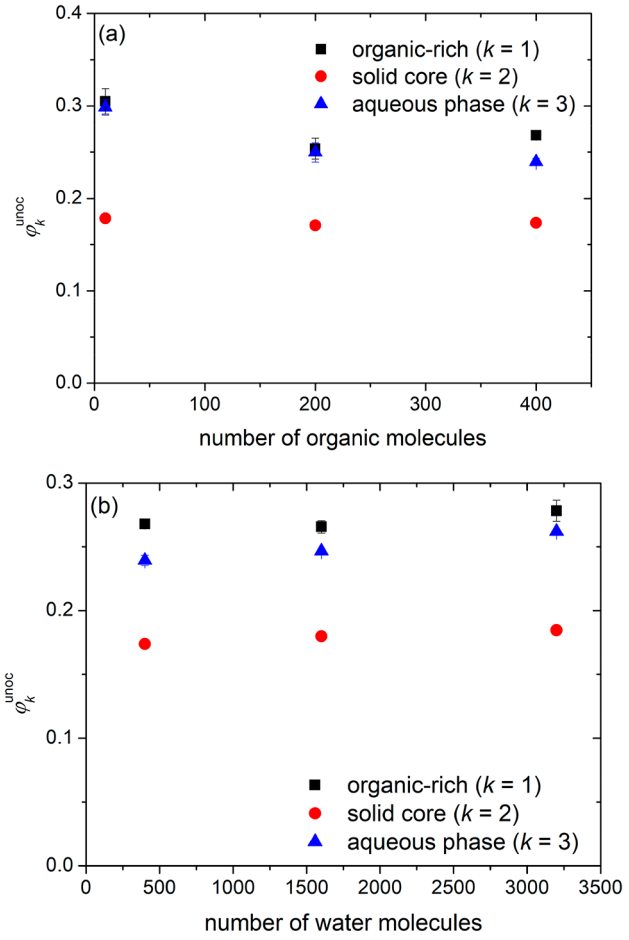

Figure 6. *Fraction* of *unoccupied volume* in the three characteristic particle regions (organic-rich, solid core, aqueous phase) as a function of the number of (a) organic and (b) water molecules.

regions characterized by very small total accessible or unoccupied volumes, for instance, the organic-rich domains in System 1 (low organic mass) or the aqueous phases in Systems 4 and 5 (high RH), suffer from large uncertainties and are presented only for completeness. The *fraction* of *unoccupied volume* in the organic phase, φ_{water}^{acc}, is on average between 0.25 and 0.27, and the lowest φ_k^{unoc} is found in the areas dominated by inorganics (0.15−0.2), implying only a tiny amount of free volume at the center of the particle where the inorganic ions prefer to reside forming a dense solid core.

Figure 7 shows the results of the geometric analysis for the *fraction* of volume *accessible* to a water penetrant ($r_p = r_w$) in the three key phases (organic-rich, solid core, aqueous). Again, except for the smallest nanoparticle (System 1), the geometric analysis reveals that clusters of *accessible volume* for the chosen penetrant exist only in organic-rich domains. These $\varphi_{organic}^{acc}$ values vary mildly between 0.008 and 0.014 and appear to be approximately 2.0−3.5 times larger than the corresponding accessible volume fraction in (e.g.,) pure melt poly(methyl methacrylate) or PMMA ($\varphi^{acc} \approx 0.004$) at $T = 400$ K,[16] due to

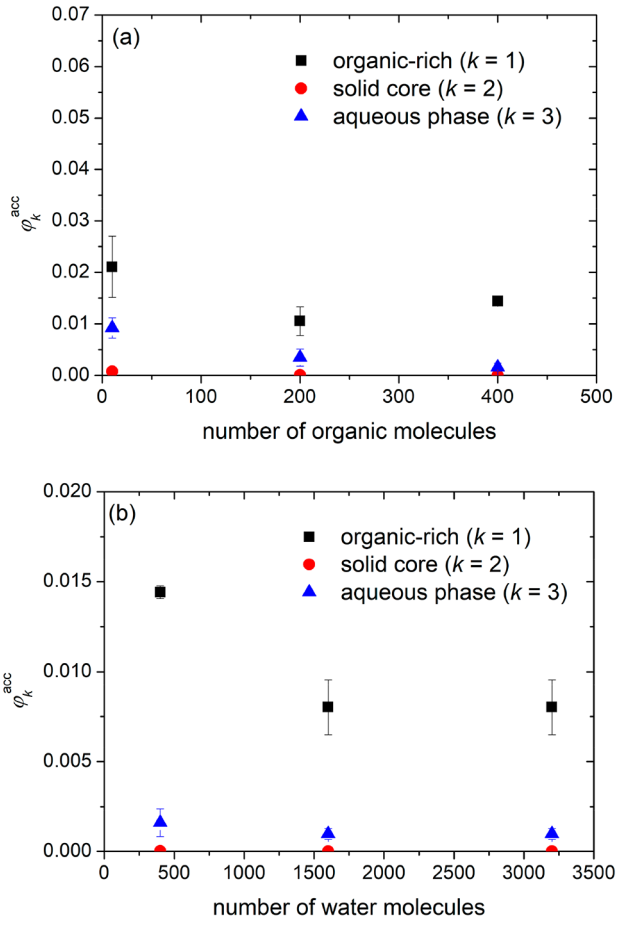

Figure 7. *Fraction* of *volume accessible* to a water molecule in the three characteristic particle regions (organic-rich, solid core, aqueous phase) as a function of the number of (a) organic and (b) water molecules.

the much shorter molecular length of CPA compared to a long PMMA chain.

Additional φ_k^{acc} results for other penetrant sizes (from $r_p = 0$ Å to $r_p = r_w$) from the geometric analysis of System 3, where the organic content is quite high, are shown in Figure 8. Obviously, φ_k^{acc} drops down to zero in the aqueous and inorganic-rich domains for penetrants of radius $r_p \geq 1$ Å, implying the complete absence of any empty space there, in the sense that not even a guest as small as a hydrogen molecule[49] can be accommodated. For the accessible volume in the aqueous phase, our results agree with those from the simulation of bulk, liquid water at the same conditions, but as we already discussed above, this is not important for the mechanism of transport as diffusion in the aqueous phase is fast and continuous and can be reliably accessed by brute-force MD.

3.4. Cavities and Their Distribution Inside the Nanoparticles. Having analyzed in detail the *total*, *unoccupied*, and *accessible volume* in each nanoparticle and their distribution in the organic-rich, inorganic or core, and aqueous phases, the next step is to study the possible formation of clusters of *accessible volume* due to pores that are connected sequentially one with the other. To make this more clear, in Figure 9, we plot the results for the volume-weighted distributions $\rho_V(V^{acc})$ (eq 22 in Mermigkis and Mavrantzas[16]) of clusters of *accessible* volume to a water molecule in Systems

https://doi.org/10.1021/acsomega.3c03293
ACS Omega 2023, 8, 33481−33492

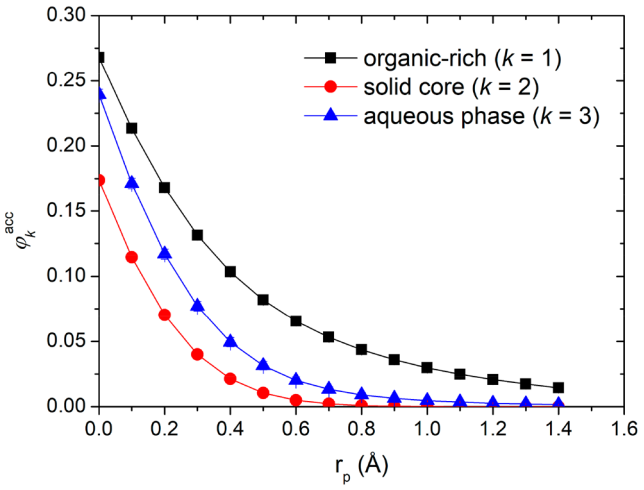

Figure 8. *Accessible* volume fraction in each one of the three characteristic particle regions (organic-rich, inorganic-rich, aqueous) as a function of penetrant radius for the nanoparticle of System 3.

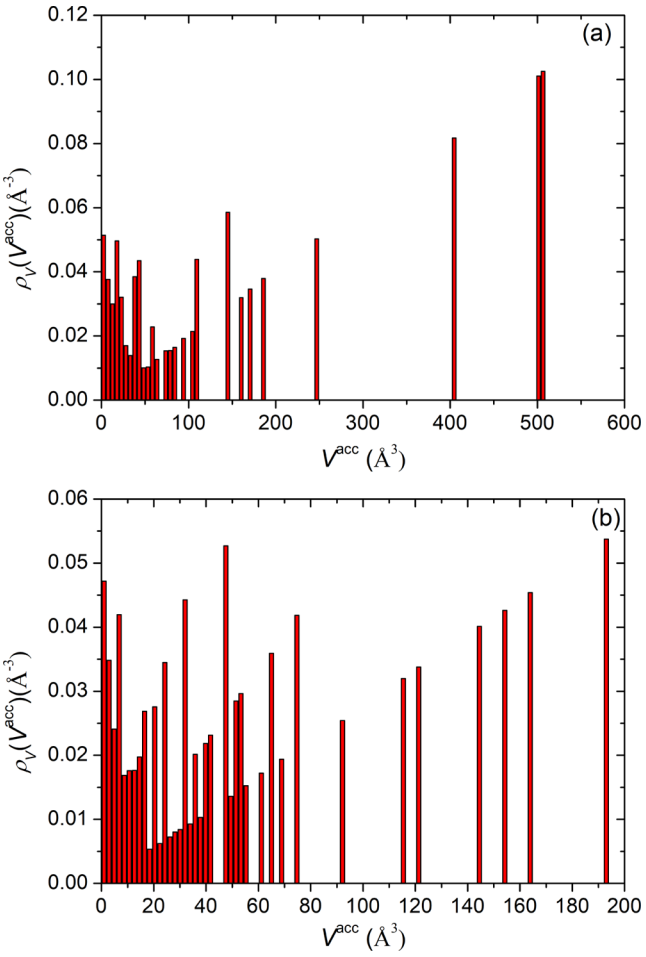

Figure 9. Volume-weighted distribution of the cluster *volume accessible* to a water molecule in the nanoparticles of (a) System 3 and (b) System 5. The figure shows the fraction of volume accessible to a water molecule in the available clusters in the two particles as a function of the volume of these clusters.

3 and 5. The total number of clusters analyzed was 142 and 198, respectively, utilizing a binning of 5 Å^3 for System 3 and 2 Å^3 for System 5. Even if System 5 is more than two times larger than System 3, the largest cluster computed (~0.5 nm^3) is identified in System 3 (Figure 9a), while the largest cavity of System 5 (Figure 9b) is less than 0.2 nm^3.

Considering that cavities appear mostly in organic-rich domains, we attribute this phenomenon to the displacement of organics to the outer area of the NPs with increasing RH (salting-out effect), which hinders the formation of a single, large cavity. To make this more clear, in Figure 10, we plot the

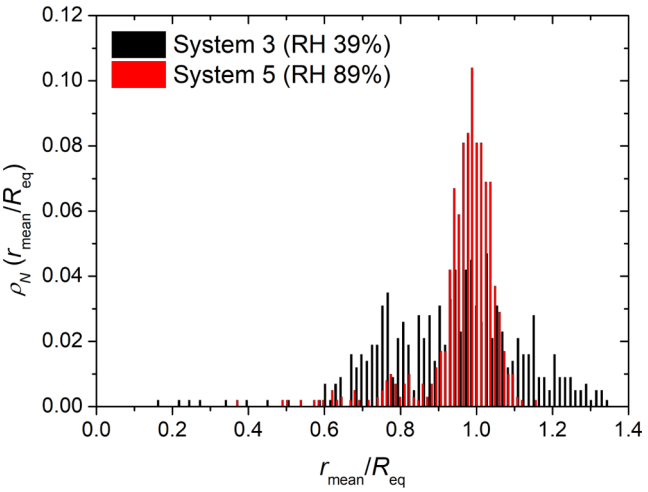

Figure 10. Number distribution of the dimensionless mean distance of the clusters *accessible* to a water molecule from the center-of-mass of the particle in Systems 3 and 5.

number distribution of the mean distance r_{mean} of the cavities from the center-of-mass of the particle, normalized with the equivalent radius R_{eq} of the particle (mathematically, r_{mean} is defined as the average distance of atoms comprising an entire cluster from the geometric center of the particle). The distribution of r_{mean}/R_{eq} is quite broad for System 3, while in System 5, cavities are preferentially located at the outer area of the particle. Values of r_{mean}/R_{eq} slightly larger than 1 are due to local deviations of the particle shape from the spherical one, which is more evident for the smaller particles (e.g., that of System 3). The largest clusters identified by the geometric analysis belong to the nanoparticle of System 3 and can be seen in Figure 11. They are primarily located at its outer area (but also at intermediate distances from its center) but not at its core which, in turn, is dominated by islands of inorganic ions and water molecules. Since these clusters belong mostly to the external area of the particle, their shape is irregular, with a mean asphericity parameter between 0.4 and 0.45. Of course, it is important to note here that the sites or clusters of free volume accessible to a penetrant (such as a water molecule) computed in the present study are based solely on geometric criteria without having taken into account additional, preferential energetic (enthalpic) interactions between the penetrant and the constituent molecules. For water, in particular, an important role in its solubility within the NP will be played by specific interactions such as hydrogen bonds with the polar groups of certain compounds of the NP, and this could be the subject of a future study.

Of interest is also to compute the characteristic penetrant radius $r_{p,c}$ for which the average number of clusters per nanoparticle reaches the maximum value. This is shown in Figure 12 and suggests a value of $r_{p,c}$ close to 0.5 Å for all

https://doi.org/10.1021/acsomega.3c03293
ACS Omega 2023, 8, 33481−33492

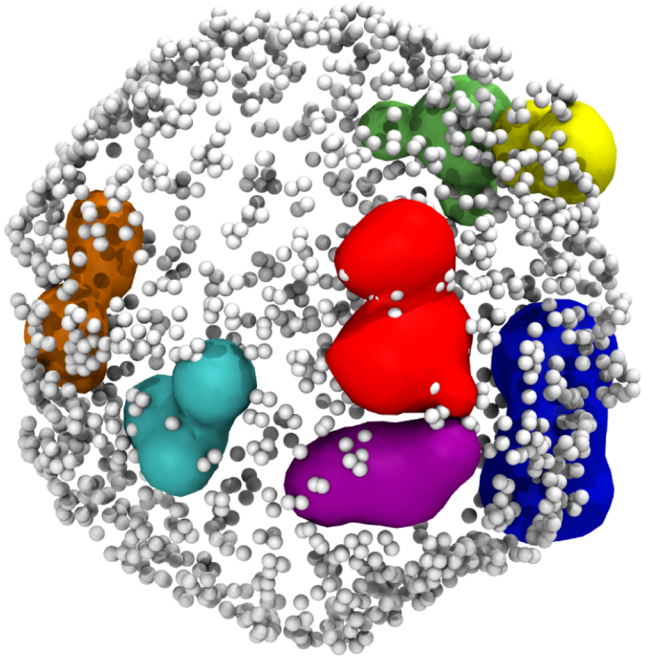

Figure 11. Visualization of the seven largest clusters accessible to water identified by the present geometric analysis in one of the configurations of the nanoparticle of System 3 (containing 69% organic mass at 39% RH). Different colors denote different clusters. The *boundary* atoms are denoted as small white beads.

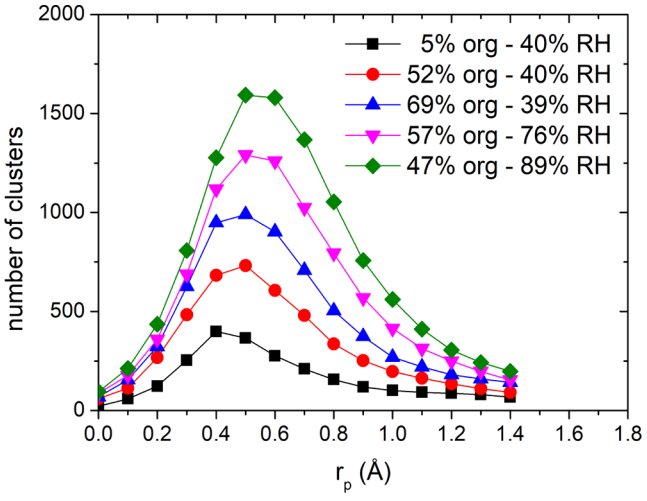

Figure 12. Average number of total clusters in the five simulated nanoparticles as a function of penetrant radius.

particles except the smallest one (System 1), for which $r_{p,c}$ = 0.4 Å. From Figure 12, we also see that larger particles include always more clusters of *volume accessible* to any penetrant with a radius equal to or smaller than that of water ($r_p \leq r_w$ = 1.4 Å). We also mention that $r_{p,c}$ is most likely a system size-dependent quantity,[12] but its value should reach an asymptote with increasing particle size while keeping its composition constant under the same temperature and pressure conditions.

Overall, the geometric analysis indicates that places where significant amounts of accessible volume are computed roughly coincide with the domains where organics prefer to reside in the NP, for all different levels of RH studied. The accessible volume, particularly in the presence of an organic coating, may enable the uptake of reactive gases and water vapor, which could impact the rate of particle growth or its heterogeneous chemistry reactivity. The organic coating does not appear to inhibit the uptake of gas molecules, although this may depend on the type of organics present.[50] On the other hand, the gradient observed in the unoccupied and accessible volumes may also suggest a gradient in water transport, which is thought to be more significant for nanosized particles.[51,52] Additionally, the dispersion of pores/cavities as described in this work, particularly at low to medium RH values, is consistent with the hopping process described by Song et al.,[21] and it could be potentially connected with particle morphology and phase state.

4. CONCLUSIONS

By subjecting model microstructures of atmospheric particles generated by detailed atomistic Molecular Dynamics simulations to Delaunay tessellation and computing their volume with Monte Carlo integration, we have been able to compute their unoccupied or free volume, as well as the cavities of free volume inside these particles, where a penetrant of a certain radius can reside. The studied particles consist of ammonium and sulfate ions, *cis*-pinonic acid, and water molecules. From the geometric analysis, we obtained results for the total volume of the particles, their equivalent diameter, and shape (the latter quantified in terms of the relative shape anisotropy parameter) that are consistent with a previous but less detailed study. The mean dimensionless asphericity showed that larger nanoparticles are quite spherical, but their surface area is slightly larger than that of the corresponding equivalent sphere due to roughness.

According to the geometric analysis, both the total *unoccupied* and the total *accessible volume fraction* of the nanoparticle to a hypothetical guest penetrant increase as the organic content increases. When the relative humidity is increased, the *unoccupied volume* increases while the *accessible volume* decreases. Most of the *accessible volume* to penetrants with size similar to that of water is found in the organic-rich regions, and these are practically the only regions where such a penetrant can be accommodated. In contrast, regions rich in inorganic ions do not contain any cavities that could host realistic penetrants (e.g., with a radius larger than 1 Å). Although the same observation applies to the aqueous domains of the particles and even to bulk liquid water, we remind the reader that the geometric analysis presented here is a static one; thus, other important diffusive mechanisms of direct relevance to microscopic transport in simple fluids, such as the fast redistribution of empty space and the rapid (practically instantaneous) formation of new cavities that lead to continuous appearance of diffusive pathways between neighboring cavities (due to high mobility of small molecules in their pure liquid state), have not been considered here.

The largest pores accessible to water were found in the medium-sized nanoparticles characterized by high levels of organic mass and low relative humidity, while at higher relative humidity, the extra presence of water molecules disturbs these clusters by pushing organic molecules (which is the only region where appreciable pores can be found) to the outer areas of the particles. In general, at lower relative humidity, diffusive pores are dispersed everywhere in the nanoparticle except its core, while at higher relative humidity, these pores are mainly located at the surface of the particle (and of course in its aqueous domains).

https://doi.org/10.1021/acsomega.3c03293
ACS Omega 2023, 8, 33481−33492

According to the present analysis, at medium-to-high levels of relative humidity, the diffusivity should be expected to be fast due to the presence of the aqueous phase. At low relative humidity, however, the diffusive motion will be more jump-like and proceed through activated hops between neighboring sorption sites such as those identified in this work, necessitating a more hierarchical simulation methodology. Thus, in a future study, the rates of transition of a given penetrant between the cavities of accessible volume identified in the present work can be estimated using transition state theory on the basis of the quasi-harmonic approximation. These can serve as input to larger-scale kinetic Monte Carlo calculations capable of tracking the long-time scale diffusive motion of these molecules inside the nanoparticle from which we can extract next their diffusivity.

■ ASSOCIATED CONTENT

Supporting Information

The Supporting Information is available free of charge at https://pubs.acs.org/doi/10.1021/acsomega.3c03293.

Figures showing the fraction of total and unoccupied volume of the nanoparticle in each of the three characteristic regions (organic-rich, solid core, aqueous phase) as a function of the number of (a) organic molecules and (b) water molecules (PDF)

■ AUTHOR INFORMATION

Corresponding Author

Vlasis G. Mavrantzas − *Department of Chemical Engineering, University of Patras, GR 26504 Patras, Greece; Institute of Chemical Engineering Sciences, FORTH-ICE/HT, Patras, GR 26504 Patras, Greece; Particle Technology Laboratory, Institute of Energy & Process Engineering, Department of Mechanical and Process Engineering, ETH Zürich, CH-8092 Zürich, Switzerland;* orcid.org/0000-0003-3599-0676; Phone: +30-6944-602580; Email: vlasis@chemeng.upatras.gr, vlasiosm@mat.ethz.ch

Authors

Panagiotis G. Mermigkis − *Department of Chemical Engineering, University of Patras, GR 26504 Patras, Greece; Institute of Chemical Engineering Sciences, FORTH-ICE/HT, Patras, GR 26504 Patras, Greece*

Katerina S. Karadima − *Department of Chemical Engineering, University of Patras, GR 26504 Patras, Greece; Institute of Chemical Engineering Sciences, FORTH-ICE/HT, Patras, GR 26504 Patras, Greece*

Spyros N. Pandis − *Department of Chemical Engineering, University of Patras, GR 26504 Patras, Greece; Institute of Chemical Engineering Sciences, FORTH-ICE/HT, Patras, GR 26504 Patras, Greece*

Complete contact information is available at: https://pubs.acs.org/10.1021/acsomega.3c03293

Notes

The authors declare no competing financial interest.

■ ACKNOWLEDGMENTS

This work was supported by the project CHEVOPIN of the Greek HFRI (agreement 1819). The authors acknowledge the computational time granted by the Greek Research & Technology Network (GRNET) in the National HPC facility−ARIS under the project names DiCoMOrA (pr010011), Multimicelles (pr012037). The authors would also like to thank Dr. Dimitrios G. Tsalikis for his contribution to the design of Figure 11.

■ REFERENCES

(1) Doolittle, A. K. Studies in Newtonian Flow. II. The Dependence of the Viscosity of Liquids on Free-Space. *J. Appl. Phys.* **1951**, *22*, 1471−1475.

(2) Turnbull, D.; Cohen, M. H. Free-Volume Model of the Amorphous Phase: Glass Transition. *J. Chem. Phys.* **1961**, *34*, 120.

(3) Turnbull, D.; Cohen, M. H. On the Free-Volume Model of the Liquid-Glass Transition. *J. Chem. Phys.* **1970**, *52*, 3038−3041.

(4) Cohen, M. H.; Grest, G. S. Liquid-glass Transition, a Free-volume approach. *Phys. Rev. B* **1979**, *20*, 1077−1098.

(5) White, R. P.; Lipson, J. E. G. Polymer Free Volume and Its Connection to the Glass Transition. *Macromolecules* **2016**, *49*, 3987−4007.

(6) Takeuchi, H.; Roe, R.; Mark, J. Molecular Dynamics Simulation of Diffusion of Small Molecules in Polymers. II. Effect of free volume distribution. *J. Chem. Phys.* **1990**, *93*, 9042−9048.

(7) Brandt, W. W. Model Calculation of the Temperature Dependence of Small Molecule Diffusion in High Polymers. *J. Phys. Chem. A* **1959**, *63*, 1080−1084.

(8) DiBenedetto, A. T. Molecular Properties of Amorphous High Polymers. An Interpretation of Gaseous Diffusion Through Polymers. *J. Polym. Sci., Part A: Gen. Pap.* **1963**, *1*, 3477−3487.

(9) Pace, R. J.; Datyner, A. Statistical Mechanical Model for Diffusion of Simple Penetrants in Polymers. I. Theory. *J. Polym. Sci., Polym. Phys. Ed.* **1979**, *17*, 437−451.

(10) Boyd, R. H.; Pant, P. V. K. Molecular Packing and Diffusion in Polyisobutylene. *Macromolecules* **1991**, *24*, 6325−6331.

(11) Arizzi, S.; Mott, P. H.; Suter, U. W. Space Available to Small Diffusants in Polymeric Glasses - Analysis of Unoccupied Space and its Connectivity. *J. Polym. Sci., Part B: Polym. Phys.* **1992**, *30*, 415−426.

(12) Greenfield, M. L.; Theodorou, D. N. Geometric Analysis of Diffusion Pathways in Glassy and Melt Atactic Polypropylene. *Macromolecules* **1993**, *26*, 5461−5472.

(13) Gusev, A. A.; Arizzi, S.; Suter, U. W.; Moll, D. J. Dynamics of Light Gases in Rigid Matrices of Dense Polymers. *J. Chem. Phys.* **1993**, *99*, 2221−2227.

(14) Gusev, A. A.; Suter, U. W. Dynamics of Small Molecules in Dense Polymers Subject to Thermal Motion. *J. Chem. Phys.* **1993**, *99*, 2228−2234.

(15) Greenfield, M. L.; Theodorou, D. N. Molecular Modeling of Methane Diffusion in Glassy Atactic Polypropylene via Multidimensional Transition State Theory. *Macromolecules* **1998**, *31*, 7068−7090.

(16) Mermigkis, P. G.; Mavrantzas, V. G. Geometric Analysis of Clusters of Free Volume Accessible to Small Penetrants and Their Connectivity in Polymer Nanocomposites Containing Carbon Nanotubes. *Macromolecules* **2020**, *53*, 9563−9583.

(17) Dodd, L. R.; Theodorou, D. N. Analytical Treatment of the Volume and Surface Area of Molecules Formed by an Arbitrary Collection of Unequal Spheres Intersected by Planes. *Mol. Phys.* **1991**, *72*, 1313−1345.

(18) Voyiatzis, E.; Böhm, M. C.; Müller-Plathe, F. A Geometric Approach to Identify Cavities in Particle Systems. *Comput. Phys. Commun.* **2015**, *196*, 247−254.

(19) Karadima, K. S.; Mavrantzas, V. G.; Pandis, S. N. Molecular Dynamics Simulation of the Local Concentration and Structure in Multicomponent Aerosol Nanoparticles Under Atmospheric Conditions. *Phys. Chem. Chem. Phys.* **2017**, *19*, 16681−16692.

(20) Karadima, K. S.; Mavrantzas, V. G.; Pandis, S. N. Insights into the Morphology of Multicomponent Organic and Inorganic Aerosols from Molecular Dynamics Simulations. *Atmos. Chem. Phys.* **2019**, *19*, 5571−5587.

(21) Song, Y. C.; Ingram, S.; Arbon, R. E.; Topping, D. O.; Glowacki, D. R.; Reid, J. P. Transient Cavity Dynamics and Divergence from the Stokes−Einstein Equation in Organic Aerosol. *Chem. Sci.* **2020**, *11*, 2999−3006.
(22) Seinfeld, J. H.; Pandis, S. N. *Atmospheric Chemistry and Physics: From Air Pollution to Climate Change*, 2nd ed.; Johh Wiley & Sons: New Jersey, 2006.
(23) Donahue, N. M.; Epstein, S. A.; Pandis, S. N.; Robinson, A. L. A Two-Dimensional Volatility Basis Set: 1. Organic-Aerosol Mixing Thermodynamics. *Atmos. Chem. Phys.* **2011**, *11*, 3303−3318.
(24) Buajarern, J.; Mitchem, L.; Reid, J. P. Characterizing the Formation of Organic Layers on the Surface of Inorganic/Aqueous Aerosols by Raman Spectroscopy. *J. Phys. Chem. A* **2007**, *111*, 11852−11859.
(25) Zobrist, B.; Marcolli, C.; Pedernera, D. A.; Koop, T. Do Atmospheric Aerosols Form Glasses? *Atmos. Chem. Phys.* **2008**, *8*, 5221−5244.
(26) Kwamena, N.-O. A.; Buajerern, J.; Reid, J. P. Equilibrium Morphology of Mixed Organic/Inorganic/Aqueous Aerosol Droplets: Investigating the Effect of Relative Humidity and Surfactants. *J. Phys. Chem. A* **2010**, *114*, 5787−5795.
(27) Virtanen, A.; Joutsensaari, J.; Koop, T.; Kannosto, J.; Yli-Pirilä, P.; Leskinen, J.; Mäkelä, J. M.; Holopainen, J. K.; Pöschl, U.; Kulmala, M.; Worsnop, D. R.; Laaksonen, A. An Amorphous Solid State of Biogenic Secondary Organic Aerosol Particles. *Nature* **2010**, *467*, 824−827.
(28) Koop, T.; Bookhold, J.; Shiraiwab, M.; Poschl, U. Glass Transition and Phase State of Organic Compounds: Dependency on Molecular Properties and Implications for Secondary Organic Aerosols in the Atmosphere. *Phys. Chem. Chem. Phys.* **2011**, *13*, 19238−19255.
(29) Bertram, A. K.; Martin, S. T.; Hanna, S. J.; Smith, M. L.; Bodsworth, A.; Chen, Q.; Kuwata, M.; Liu, A.; You, Y.; Zorn, S. R. Predicting the Relative Humidities of Liquid-Liquid Phase Separation, Efflorescence, and Deliquescence of Mixed Particles of Ammonium Sulfate, Organic Material, and Water Using the Organic-to-Sulfate Mass Ratio of the Particle and the Oxygen-to-Carbon Elemental Ratio of the Organic Component. *Atmos. Chem. Phys.* **2011**, *11*, 10995−11006.
(30) Zuend, A.; Seinfeld, J. H. Modeling the Gas-particle Partitioning of Secondary Organic Aerosol: The Importance of Liquid-Liquid Phase Separation. *Atmos. Chem. Phys.* **2012**, *12*, 3857−3882.
(31) Pöhlker, C.; Wiedemann, K. T.; Sinha, B.; Shiraiwa, M.; Gunthe, S. S.; Smith, M.; Su, H.; Artaxo, P.; Chen, Q.; Cheng, Y.; Elbert, W.; Gilles, M. K.; Kilcoyne, A. L. D.; Moffet, R. C.; Weigand, M.; Martin, S. T.; Pöschl, U.; Andreae, M. O. Biogenic Potassium Salt Particles as Seeds for Secondary Organic Aerosol in the Amazon. *Science* **2012**, *337*, 1075−1078.
(32) Song, M.; Marcolli, C.; Krieger, U. K.; Zuend, A.; Peter, T. Liquid-Liquid Phase Separation in Aerosol Particles: Dependence on O:C, Organic Functionalities, and Compositional Complexity. *Geophys. Res. Lett.* **2012**, *39*, L19801.
(33) You, Y.; Smith, M. L.; Song, M.; Martin, S. T.; Bertram, A. K. Liquid−Liquid Phase Separation in Atmospherically Relevant Particles Consisting of Organic Species and Inorganic Salts. *Int. Rev. Phys. Chem.* **2014**, *33*, 43−77.
(34) Veghte, D. P.; Bittner, D. R.; Freedman, M. A. Cryo-Transmission Electron Microscopy Imaging of the Morphology of Submicrometer Aerosol Containing Organic Acids and Ammonium Sulfate. *Anal. Chem.* **2014**, *86*, 2436−2442.
(35) You, Y.; Bertram, A. K. Effects of Molecular Weight and Temperature on Liquid−Liquid Phase Separation in Particles Containing Organic Species and Inorganic Salts. *Atmos. Chem. Phys.* **2015**, *15*, 1351−1365.
(36) Losey, D. J.; Parker, R. G.; Freedman, M. A. pH Dependence of Liquid−Liquid Phase Separation in Organic Aerosol. *J. Phys. Chem. Lett.* **2016**, *7*, 3861−3865.
(37) Song, M.; Liu, P.; Martin, S. T.; Bertram, A. K. Liquid−Liquid Phase Separation in Particles Containing Secondary Organic Material Free of Inorganic Salts. *Atmos. Chem. Phys.* **2017**, *17*, 11261−11271.
(38) Freedman, M. A. Phase Separation in Organic Aerosol. *Chem. Soc. Rev.* **2017**, *46*, 7694−7705.
(39) Riemer, N.; Ault, A. P.; West, M.; Craig, R. L.; Curtis, J. H. Aerosol Mixing State: Measurements, Modeling, and Impacts. *Rev. Geophys.* **2019**, *57*, 187−249.
(40) Freedman, M. A. Liquid−Liquid Phase Separation in Supermicrometer and Submicrometer. *Acc. Chem. Res.* **2020**, *53*, 1102−1110.
(41) Gorkowski, K.; Donahue, N. M.; Sullivan, R. C. Aerosol Optical Tweezers Constrain the Morphology Evolution of Liquid-Liquid Phase-Separated Atmospheric Particles. *Chem* **2020**, *6*, 204−220.
(42) Huang, Y.; Mahrt, F.; Xu, S.; Shiraiwa, M.; Zuend, A.; Bertram, A. K. Coexistence of Three Liquid Phases in Individual Atmospheric Aerosol Particles. *Proc. Natl. Acad. Sci. U.S.A.* **2021**, *118*, No. e2102512118.
(43) Gaikwad, S.; Jeong, R.; Kim, D.; Lee, K.; Jang, K.-S.; Kim, C.; Song, M. Microscopic Observation of a Liquid-liquid-(semi)solid Phase in Polluted $PM_{2.5}$. *Front. Environ. Sci.* **2022**, *10*, No. 947924.
(44) Schervish, M.; Shiraiwa, M. Impact of Phase State and Non-Ideal Mixing on Equilibration Timescales of Secondary Organic Aerosol Partitioning. *Atmos. Chem. Phys.* **2023**, *23*, 221−233.
(45) Tanemura, M.; Ogawa, T.; Ogita, N. A New Algorithm For 3-Dimensional Voronoi Tessellation. *J. Comput. Phys.* **1983**, *51*, 191−207.
(46) https://www.sigmaaldrich.com/GR/en/product/aldrich/110108 (accessed on 27 June 2023).
(47) https://pubchem.ncbi.nlm.nih.gov/#query=crystalline%20ammonium%20sulfate (accessed on 27 June 2023).
(48) https://www.thermexcel.com/english/tables/eau_atm.htm (accessed on 27 June 2023).
(49) Mandal, P. K.; Arunan, E. Hydrogen Bond Radii for the Hydrogen Halides and van der Waals Radius of Hydrogen. *J. Chem. Phys.* **2001**, *114*, 3880−3882.
(50) Li, W.; Pak, C. Y.; Wang, X.; Tse, Y.-L. S. Uptake of Common Atmospheric Gases by Organic-Coated Water Droplets. *J. Phys. Chem. C* **2019**, *123*, 18924−18931.
(51) Preston, T. C. Non-Fickian Diffusion in Viscous Aerosol Particles. *Can. J. Chem.* **2022**, *100*, 168−174.
(52) Preston, T. C.; Zuend, A. Equilibration Times in Viscous and Viscoelastic Aerosol Particles. *Environ. Sci.: Atmos.* **2022**, *2*, 1376−1388.

https://doi.org/10.1021/acsomega.3c03293
ACS Omega 2023, 8, 33481−33492